The JET ECE Heterodyne Radiometer and Investigations of Fast Phenomena

D V Bartlett, A E Costley, S E Jones[1], L Porte,
R J Smith, A Zolfaghari[1]

JET Joint Undertaking, Abingdon, Oxon, OX14 3EA.
[1] MIT Plasma Fusion Center, Cambridge, MA, USA.

THE JET ECE HETERODYNE RADIOMETER AND INVESTIGATIONS OF FAST PHENOMENA

D V Bartlett, A E Costley, S E Jones*, L Porte, R J Smith, A Zolfaghari*

JET Joint Undertaking, Abingdon, Oxon. OX14 3EA, UK
** MIT Plasma Fusion Center, Cambridge, MA 02139, USA*

ABSTRACT

In this paper, the design and performance characteristics of the JET heterodyne radiometer are reviewed, and some novel aspects of the instrument are described. Areas where the radiometer could benefit from further improvement are highlighted, and those improvements currently in progress are discussed. Some measurements which demonstrate the radiometer's power as a diagnostic of fast phenomena are presented.

(1) INTRODUCTION

A heterodyne radiometer is the most recent addition to the JET ECE measurement system. The original 8 channel radiometer has been presented at a previous workshop in this series [1], and progress in the development of the upgraded instrument has been briefly described [2]. The upgraded radiometer has now been operational for some time. It has proven to be a powerful tool for studying the temporal evolution of the electron temperature at fixed radii with good spatial and temporal resolutions.

The upgraded instrument has wider frequency coverage than the original, with more simultaneous observation channels, while maintaining its high sensitivity and excellent spectral resolution. Recently, it has been used with a fast (up to 1 MHz) data acquisition system.

In this paper an overview of the upgraded radiometer is given and some of the novel features of the design are described. Our experience of operating the instrument is summarized. Some examples of observations of fast phenomena are presented, and the possible interpretation of these phenomena is discussed. Finally, further improvements which are planned to be made during the present shutdown of JET are described.

(2) THE UPGRADED JET ECE HETERODYNE RADIOMETER

The upgraded heterodyne radiometer is shown schematically in Figure 1. The architecture is essentially the same as that of the original instrument: broadband mixers with fixed frequency local oscillators and an intermediate frequency (IF) chain split into a number of frequency channels. The number of mixers has now been increased to four to achieve the wider spectral coverage.

ECE is collected and transmitted by one of the channels of the JET oversized (S-band/WG10) waveguide system [3]. On entering the radiometer, the power is divided four ways by three non-polarizing beamsplitters which are described in more detail below. This permits the four mixers to make simultaneous measurements of the radiation from the one input waveguide. The input waveguide carries both orthogonal linear polarizations from the plasma, and the polarization selection is made just before the mixers. This allows each mixer to be used independently for either first harmonic (ordinary mode) or second harmonic (extraordinary mode) measurements, thus increasing the accessible range of major radius at various values of toroidal field. The polarization selectors are also described in more detail below.

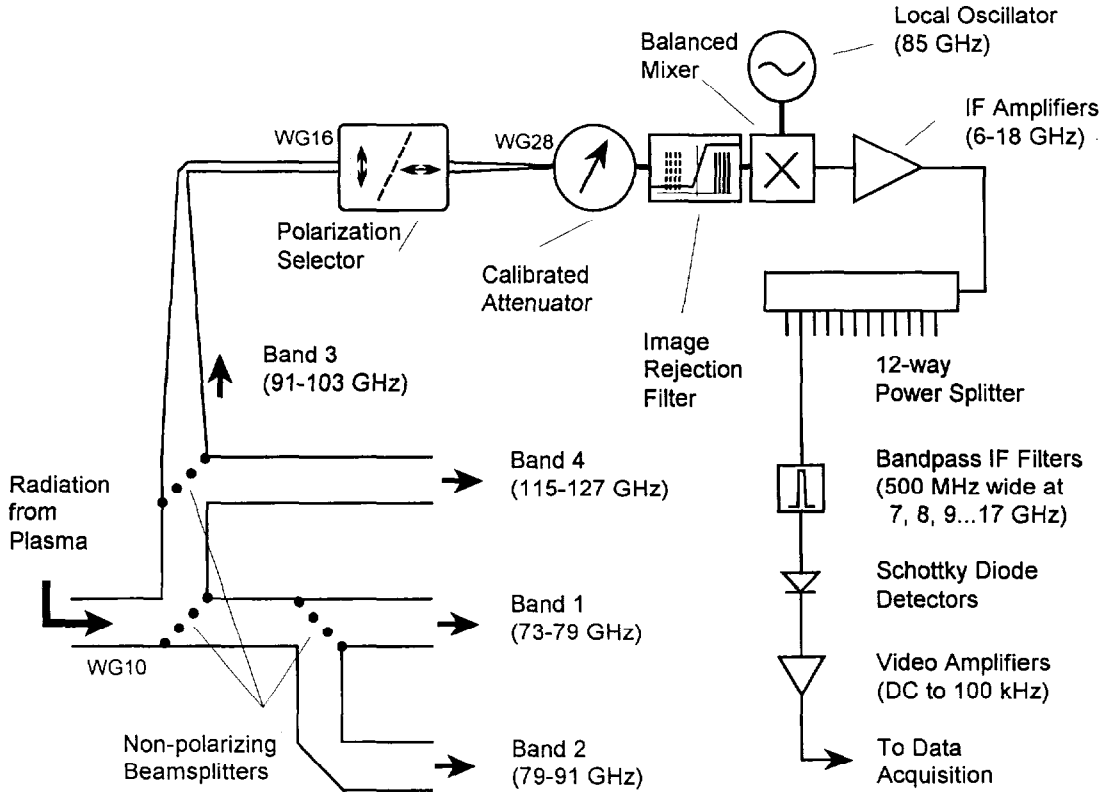

Figure 1: *Schematic of the upgraded heterodyne radiometer. Incoming radiation is split four ways by the non-polarizing beamsplitters. Only one of the four radiometer bands is illustrated, the others have the same architecture. Each band consists of a polarization selector, mixer, IF amplifier and power splitter, followed by bandpass filters, video detectors and amplifiers.*

The mixers are commercially supplied balanced mixers with integral lower sideband rejection filters and fixed frequency Gunn diode local oscillators. The local oscillator frequencies, IF bandwidths and other parameters are given in Table I.

The reason for the gap in frequency between bands 3 and 4 is because the 115 to 127 GHz range is more useful than the 103 to 115 GHz range for the most commonly used values of toroidal field in JET. This is illustrated in Figure 2, which shows the major radius range covered by the radiometer as a function of the on-axis (R = 2.96 m) toroidal magnetic field. This calculation has been made using the vacuum (1/R) magnetic field profile: when plasma generated magnetic fields are included the radii are displaced outwards by up to 0.20 m. The plasma inner and outer limits are usually about 1.95 and 4.10 m, and the plasma

centre at about 3.10 m. This figure shows that the radiometer can make measurements of optically thick first or second harmonic emission over a wide range of radii for toroidal fields between 3.4 tesla (the upper limit in JET) and 1.5 tesla. The inner radius limit for the second harmonic is due to harmonic overlap. During high-β, low toroidal field (~1 tesla) experiments, the optically grey third harmonic has also been used (see Section 4).

Following IF amplification, the IF power is split into eight (or twelve) channels which then pass through bandpass filters whose centre frequencies are spread across the IF band. The result is an instrument with 44 fixed frequency channels spread over the ranges 73 to 103 GHz and 115 to 127 GHz.

The Schottky diode detectors are followed by either the standard data acquisition system or a recently installed fast acquisition. The standard acquisition has video amplifiers with remotely programmable gain and bandwidth (from DC up to a maximum of 100 kHz), and CAMAC ADCs with 16 ksample memory per channel and sample rates up to 125 kHz. The fast system uses a GPIB interface between CAMAC ADCs and a PC, with data stored locally on a WORM optical disk drive. This acquisition has 128 ksample memory in each of 12 channels, and sample rates up to 1 MHz. Since it is operated in parallel with the standard acquisition, the low frequency limit of the video amplifiers in the fast system is usually set to 500 Hz, to improve dynamic range. The results reported in Section 4 were obtained mainly with the fast data acquisition.

TABLE I: JET Heterodyne radiometer parameters

	Band 1	Band 2	Band 3	Band 4
Local oscillator frequency (GHz)	67	73	85	109
IF bandwidth (GHz)	6 to 12	6 to 18	6 to 18	6 to 18
RF frequency coverage (GHz)	73 to 79	79 to 91	91 to 103	115 to 127
Number of IF channels	8	12	12	12
IF filter spacing (GHz)	0.82	1.00	1.00	1.00
IF filter width (GHz)	0.25	0.50	0.50	0.50
Typical major radius resolution (m) †	≈0.05	≈0.05	≈0.05	≈0.05
System noise (as ΔT_e (eV) in the plasma)‡	≈30	≈30	≈30	≈30
Limiting S/N ratio‡	160	220	220	220

† see text for detailed discussion. ‡ assuming a 10 kHz video bandwidth (see text).

The values of major radius resolution in Table I are calculated taking into account the IF filter widths and estimates (at the plasma centre) of both relativistic broadening for typical T_e (a few keV) and Doppler broadening due to the antenna pattern divergence angle. Near the outboard edge of the plasma, where T_e is lower and the rays in the antenna pattern are closer to perpendicular to the magnetic field, the major radius resolution is less than 0.03 m. Measurements which confirm the spatial resolution actually achieved by the radiometer, and a discussion of the effects of the antenna spot size on the spatial averaging volume, are given in Section 3. The total system noise has been converted into an equivalent temperature in the

plasma using the measured system responsivity, and assuming a 10 kHz video bandwidth. The values in the table can be regarded as a minimum detectable T_e change. Generally, the signal-to-noise ratio is limited by the well known effect of the thermodynamic fluctuations in the black-body radiation. The values quoted in the table are calculated using the usual expression, $(B_{IF}/B_V)^{1/2}$ [4], where B_{IF} is the IF filter bandwidth and B_V is the video bandwidth, which for the values in the table is again taken to be 10 kHz.

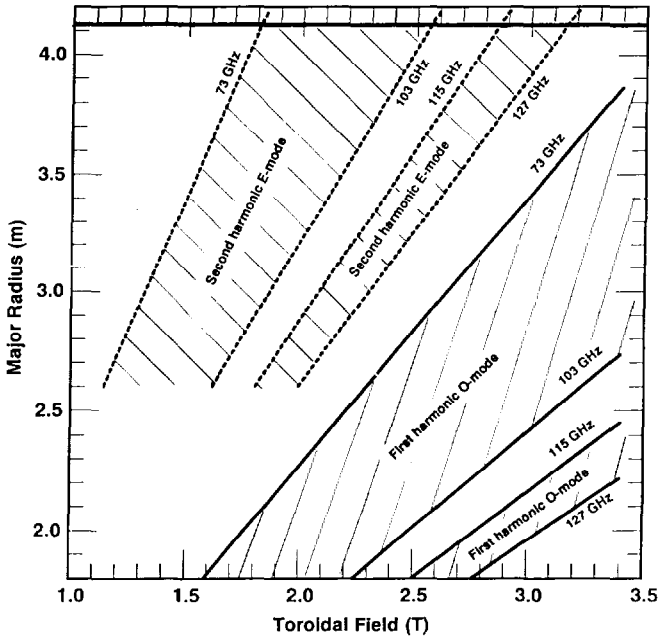

Figure 2: *The radiometer channel locations in major radius, as a function of the toroidal magnetic field at R=2.96 m. The spatial profile of the toroidal field is assumed to vary as 1/R (ie. it does not take into account the plasma generated fields). The upper two shaded zones show the radii accessible to the radiometer when measuring second harmonic emission. The gap between the two zones is due to a frequency gap between bands 3 and 4, and the inner radius limit is set by harmonic overlap. The lower two zones correspond to the first harmonic.*

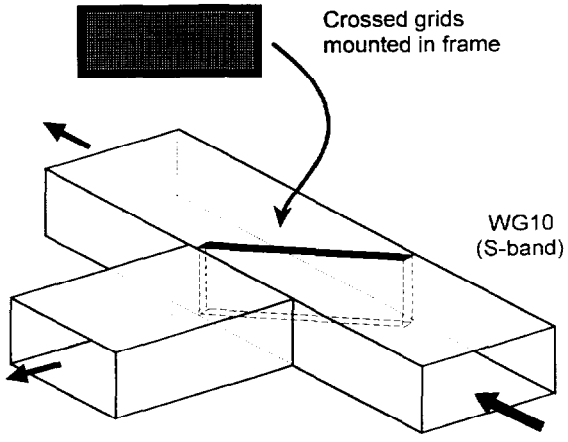

Figure 3: *Schematic showing the non-polarizing beamsplitter assembly. Cross-wound wire grids are mounted in a frame which fits closely into a groove in the waveguide wall. Each of the two orthogonal windings splits the power in one polarization.*

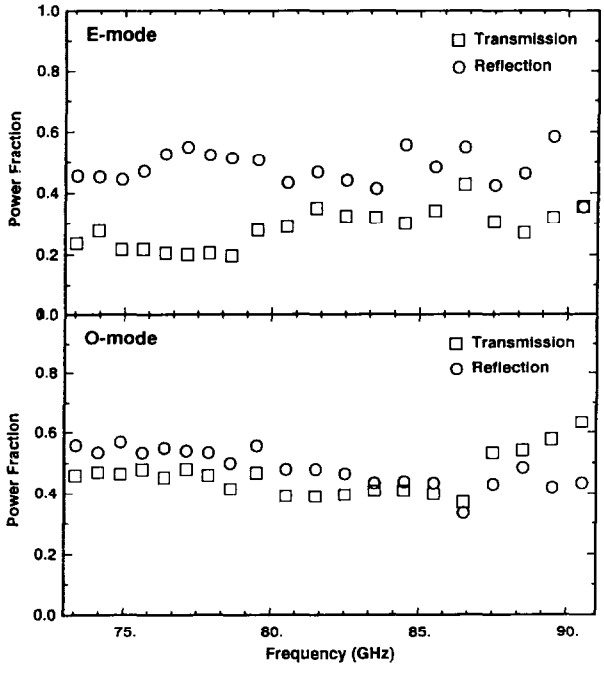

Figure 4: *Measured performance of the non-polarizing beamsplitters. The spacing of the windings is not optimum for the E-mode case.*

The non-polarizing beamsplitters used to divide power between the four mixers are shown schematically in Figure 3. An S-band waveguide T-junction is machined in a block of aluminium, with a rectangular cross-section groove cut into the walls at 45° to the waveguide axis. The groove penetrates all the way through the waveguide wall on one side so that a matching frame can be inserted. The frame and groove are matched to a close tolerance, so that when in place the frame re-creates a continuous waveguide wall. This device can be used either as a waveguide switch (an empty frame allowing radiation to pass straight through or a mirror making a mitre bend), or as a beamsplitter. In the radiometer, coarsely spaced, crossed wire grids are used as beamsplitters. The spacing of each of the two orthogonal windings is chosen to give approximately equal transmission and reflection for one polarization (this winding being transparent to the other polarization). The measured performance of the beamsplitters currently in use is shown in Figure 4. Although the measurements have modest accuracy (~20%) it is apparent that while the O-mode performance of the beamsplitters is satisfactory, in the E-mode there is an imbalance between reflection and transmission which is probably due to an inappropriate choice of wire spacing.

The polarization selectors employ a similar beamsplitter block, in X-band/WG16 waveguide, but with a uni-directional wire grid acting as a polarizing beamsplitter. The two orthogonal polarizations pass into tapers which convert from WG16 to fundamental waveguide (WG26 or WG28, depending on the band). The taper carrying radiation which has its E-vector parallel to the longer side of the WG16 waveguide (the E-mode, transmitted by the grid) inverts the aspect ratio of the guide as it tapers down to fundamental waveguide. Thus, both polarizations in the oversized waveguide arrive at the fundamental waveguide with their E-vectors in the correct orientation to propagate. After a waveguide twist in one guide to bring them both to the same orientation, a remotely controlled rotary waveguide switch is used to pass the required polarization to the mixer.

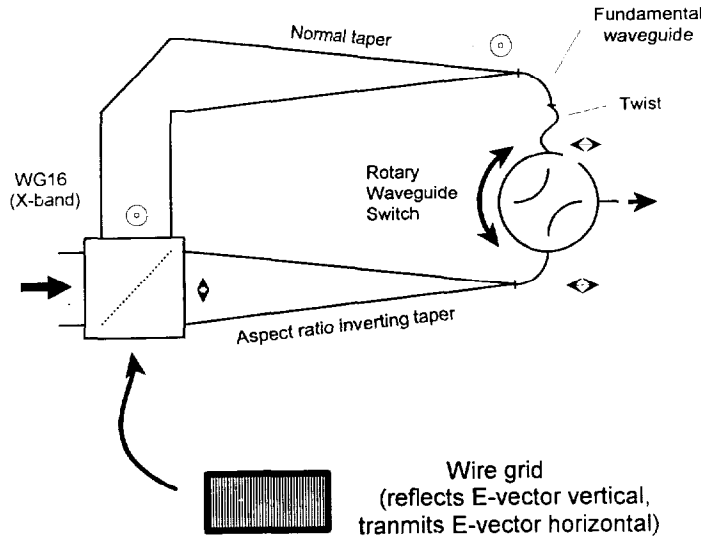

Figure 5: *Schematic of the polarization selectors. The E-mode (double headed arrow) is transmitted by the grid, and passes through a taper which inverts the aspect ratio of the guide so that it is in the correct orientation for the fundamental waveguide. The O-mode taper does not invert the aspect ratio, and a waveguide twist re-orients the guide to enter the rotary switch.*

(3) OPERATIONAL EXPERIENCE

Experience of operating the radiometer has demonstrated that it does indeed achieve its expected performance in several important respects, but also shows that in some areas further improvement is needed. This section summarizes some of the results of this experience.

In a variety of measurements, significant variation between the signals recorded in several adjacent channels of the radiometer is observed. This has been noted particularly in measurements of MHD oscillations around rational magnetic surfaces (for $q \geq 2$) and at the plasma edge. The observations of edge localized modes (ELMs) presented in Section 4 are an example of the latter. This demonstrates unambiguously that the spatial resolution is at least as good as the estimates given in Table I. However, such localization has been observed only on the outboard side, at greater than about half-radius. Further inboard it is expected that the antenna spot size effectively limits the spatial resolution. The volume of plasma over which the T_e measurements are integrated is a thin vertical disk with diameter determined by the antenna pattern and thickness by the radial resolution. Around the plasma centre, and on the inboard side (where the antenna pattern has expanded), this disk intersects a wider range of magnetic flux, or equi-temperature, surfaces than at the outboard side. The antenna spot size at the plasma centre is estimated to be about 0.22 m FWHM, so taking the plasma elongation (typically $\approx$1.3) into account, the extremities of the integration volume correspond to a minor radius resolution in the mid-plane of ~0.17 m. At half radius the corresponding minor radius resolution due to this effect is ~0.04 m, and it becomes negligible near the plasma edge. To reduce this degradation of the radiometer's resolution, an improved optical system is being installed, as described in Section 5.

Absolute spectral calibration of heterodyne radiometers using thermal sources is significantly easier than it is for the other widely used multi-channel instruments (grating polychromators and Fabry-Perot interferometers) for two reasons: (i) higher sensitivity, and (ii) no higher-order response requiring efficient filters to remove high frequency radiation. The difficulty with the JET instrument is that if all the channels are calibrated sequentially, then the total measurement time becomes very long. In principle, this can be overcome by calibrating all channels simultaneously, giving a multiplex advantage analogous to that of the Michelson interferometer. The optimum calibration technique is to use digital signal averaging on the waveform generated by a mechanical chopper placed directly in front of the calibration source. To avoid the expense of a large number of such signal averagers, we have constructed a multiplexer which rapidly switches between all the channels of one band a number of times during each period of the chopper waveform. Since the chopper waveform is low frequency (~15 Hz), a single signal averager operating at ~10 kHz can make 50 samples in each of 12 channels during each chopper period. By ensuring that the multiplexing is synchronized to the chopper, the signals from the individual channels can be separated by software after the averaging is completed.

To date, the calibration stability of the JET radiometer has been limited by frequent small modifications to the system and by a lack of temperature stabilization. It has therefore been necessary to make use of cross-calibration against the absolutely calibrated Michelson interferometer. While this gives absolute temperatures which are sufficiently accurate ($\pm$10%) for many purposes, it is difficult to achieve a relative calibration error between radiometer channels which is small enough to allow good reconstruction of profiles. The causes of this

difficulty are the very different spectral and temporal resolutions of the two instruments. Experience has shown that the best results are obtained using plasma pulses with a time dependent toroidal magnetic field, the cross-calibration of each channel being made when it is at the centre of the T_e profile.

An alternative method of obtaining a relative channel-to-channel calibration was first proposed by Uchino [5]. This method again uses pulses with a decaying toroidal magnetic field. It relies on the assumption that the T_e profile has the same symmetry as the T_e variations caused by the sawtooth oscillations. The ratio of the signal from two radiometer channels which are on either side of the plasma centre is calculated as a function of time. When the perturbation of this ratio by sawtooth oscillations disappears, the channels are assumed to be observing the same T_e and a relative calibration is obtained. This method has been applied to the upgraded radiometer to make relative calibration of up to 29 channels using one plasma pulse. By examining the consistency of the calibration factors of a series of channels when they are combined in various ways, it is estimated that the channel-to-channel error is less than ±2% across all the calibrated channels. This is confirmed by the fact that the T_e profiles reconstructed from these channels are generally smooth.

(4) OBSERVATIONS OF FAST PHENOMENA

As examples of the radiometer's ability to measure fast, spatially localized phenomena, we present two sets of observations with a brief discussion of their possible interpretation.

ELMs and non-thermal edge emission during H-modes

The good spatial resolution of the radiometer makes it well suited to the measurement of ECE from the plasma edge where spatial scale lengths can be very small. The instrument has previously been used to study the evolution of the edge T_e profile during H-modes to within 0.05 to 0.1 m of the separatrix [6]. An outer limit for reliable T_e measurements arises because of the presence during H-modes of enhanced emission at, and just below, frequencies normally associated with the extreme edge of the profile [7].

The enhanced emission takes the form of a steady-state "hump" on the emission profile as illustrated in Figure 6, which shows second harmonic E-mode spectra. The steeply rising intensity on the high frequency side is optically thick second harmonic emission from the steep edge temperature profile. The slowly rising level at low frequencies is due to overlap of the first harmonic which is on the inboard side. The "hump" always appears at the L-to-H transition and remains throughout the H-mode phase.

In these H-mode discharges, Edge Localized Modes (ELMs) are observed on the edge ECE signals as brief, very intense bursts in the same range of frequency as the hump. The bursts consist of a series of rapid spikes, a more complex structure than that of the D_α signals. The onset of the burst is not simultaneous in all the edge radiometer channels, but generally shows a rapid progression from higher to lower ECE frequencies.

Figure 7 shows the time history of the D_α signal and four radiometer channels for two ELMs in one discharge. The radiometer channels are located at radii between 3.93 m and 4.02 m (ie. from about the separatrix radius to 0.1 m inboard) and the data sampling rate is 200 kHz. The spikes occur at the same radiation frequencies as the non-thermal hump, and

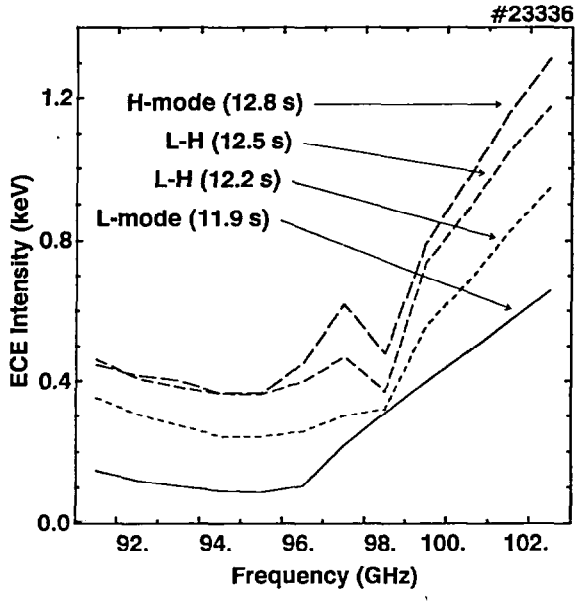

Figure 6: E-mode spectra obtained by taking data from 12 radiometer channels at several times during the L-to-H transition. The intensities are given as radiation temperature. The signal at the higher frequencies is edge second harmonic while that at lower frequencies is first harmonic from the inboard side. The "hump" of enhanced emission at ≈97 GHz appears only during the H-mode phase.

sometimes extend to slightly higher frequencies. The intensity of the spikes saturates the detection system at a radiation temperature of ~10 keV. The negative saturation of the signal sometimes seen after the ELM is caused by high-pass filtering. The D_α signal shows that an ELM occurs at the same time as the burst of ECE, but it is recorded with insufficient time resolution to detect any fine structure of the kind visible on the ECE. Although the magnetics and density reflectometer diagnostics frequently show precursor oscillations leading up to the ELMs, they are not seen on the ECE.

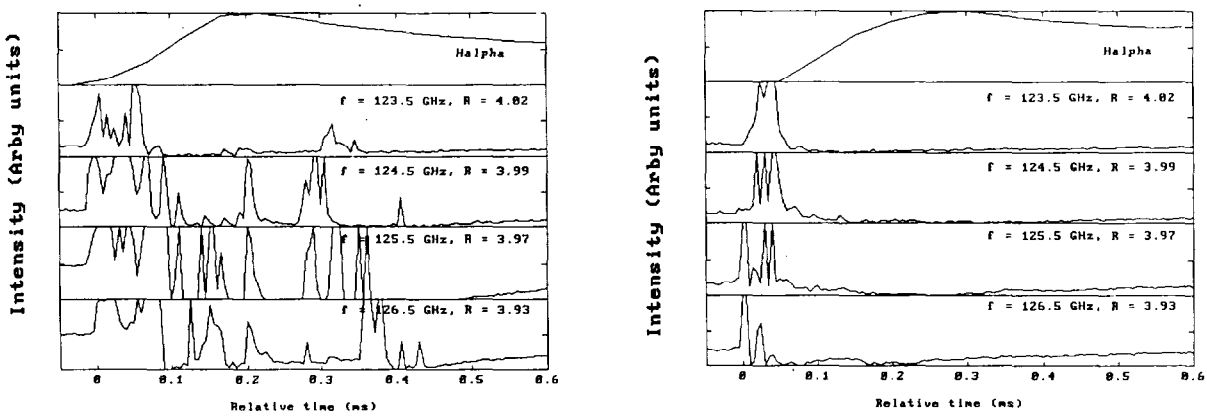

Figure 7: Time evolution of ECE in four radiometer channels for two ELMs in the same discharge (#26148), together with the D_α signal. The fast sample rate (200 kHz) allows both the channel-to-channel variation, and the variability between ELMs to be clearly seen.

The onset of the ECE ELM bursts can be difficult to identify precisely, but it is generally not exactly simultaneous in all the edge radiometer channels. There is considerable variation in the inter-channel delay time of the ELM onset from one ELM to another, so we use discharges with a large number of ELMs and make an average over them. Figure 8 plots the average start and end times of 65 ELMs in one discharge (with respect to the start time in the lowest frequency channel) as a function of emission frequency. There is a trend of increasing start time delay as the radiation frequency increases. The end time shows very large

variability, but there is a marked tendency for the ELM duration to fall with increasing radiation frequency.

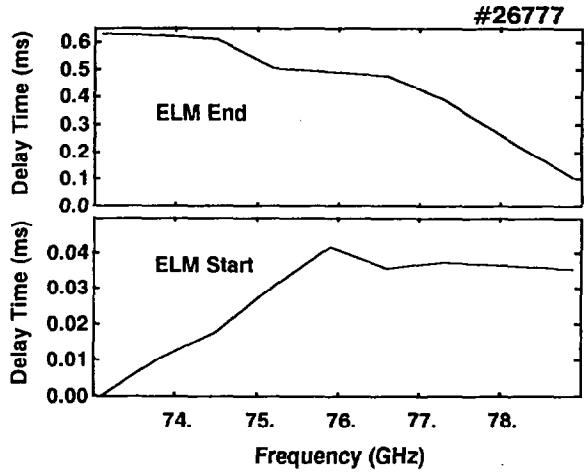

Figure 8: Start and end time of the ELM burst as a function of radiation frequency. The time origin is taken as the start time in the lowest frequency channel, and the results from a large number of ELMs in one discharge have been averaged.

To determine the spatial location of the electrons generating the hump and the ELM spikes, we have analysed the behaviour of the emission in two particular circumstances: during a brief spike which is frequently observed at the time of the sawtooth collapse in the plasma centre, and during a high density phase, which brings the upper cut-off layer near the plasma edge [7]. The spike is simultaneous with the sawtooth collapse at the plasma centre, and clearly separated from the heat pulse which propagates to the edge. The electrons generating the spike must therefore be near the plasma centre and have sufficient energy to give a relativistic downshift to a range of edge frequencies. The mechanism by which this radiation spike is generated is not well understood, but its rapidly changing intensity across the radiometer channels can be used to estimate the optical depth profile in the edge region. In these plasmas, with steep edge gradients, the transition from optically thin to optically thick occurs over only one or two radiometer channels (~0.05 m). The hump is located at frequencies for which the plasma is optically thin, immediately below this transition. The second analysis relies on the fact that these H-mode discharges have a very steep edge density profile and a high central density. If the density rises above 10^{20} m^{-3}, the upper cut-off layer moves rapidly towards the plasma edge. Since radiation emitted inboard of the cut-off layer cannot propagate to the receiving antenna on the outboard side, the falling intensity of the hump during this time shows where the emitting electrons are located. The intensity of the hump starts to be affected when the cut-off is within 0.3-0.4 m of the separatrix, and it almost disappears when the cut-off is 0.05-0.1 m from the separatrix.

Various mechanisms which might produce the non-thermal hump in the emission profile have been investigated [8]. The only explanation we have found to fit the observations is the existence of a small population of moderately suprathermal electrons in the edge region (ie. within 0.3-0.4 m of the separatrix). A limited energy range would give a small relativistic frequency downshift, corresponding to the observed emission frequency of the hump and the ELMs. The appearance of the hump during the H-mode may be due to an increase in their density, resulting from reduced outward diffusion of suprathermals through the edge transport barrier. The ELM spikes could then be explained by pitch-angle scattering of some of the suprathermals during the ELM instability, followed by their ejection from the plasma along with some of the thermal electrons. The measured spectra have been successfully modelled [7] assuming a parallel energy of the electrons limited to 60 keV, a Maxwellian distribution of

perpendicular energy at around the local plasma temperature (2-3 keV), and a density which is adjusted to fit the measured intensity of the hump (typically $<10^{-4}$ of the thermal electron density).

The frequency dependent start time of the ECE burst is not necessarily due to radial propagation of the ELM itself, since the suprathermal emission is spectrally broadened. Alternative explanations are a time evolution of the suprathermal distribution function, or radial propagation of the fall in thermal plasma density due to the ELM, which would vary the frequency at which the plasma becomes optically thick.

High frequency oscillations in high-β discharges

In tokamak plasmas with high β and large pressure gradients, a variety of MHD modes including ballooning modes can be destabilized. Pressure perturbations due to these modes can produce fluctuations in T_e which can be related to the frequency spectrum and spatial structure of such modes [9]. We present here some examples of radiometer observations of high frequency oscillations in low toroidal field high-β plasmas near the Troyon limit, and describe briefly the techniques used to analyse the large quantities of data which the radiometer and fast acquisition system can generate.

The toroidal magnetic field was 1.1 tesla, and the radiometer was set to measure third harmonic extraordinary mode, which had an optical depth of about 0.7. The limited optical depth means that wall reflections will limit the spatial localization of the measurement. However, the first reflection, from the smooth inner wall of the torus, should be reasonably well collimated, so it is estimated that about 75% ($\equiv 1 - e^{-1.4}$) of the observed intensity originates from a well defined antenna spot. Because of the extra propagation path through the plasma, this spot may be up to 0.7 m in diameter. This limited space localization must be considered in any quantitative analysis of this data.

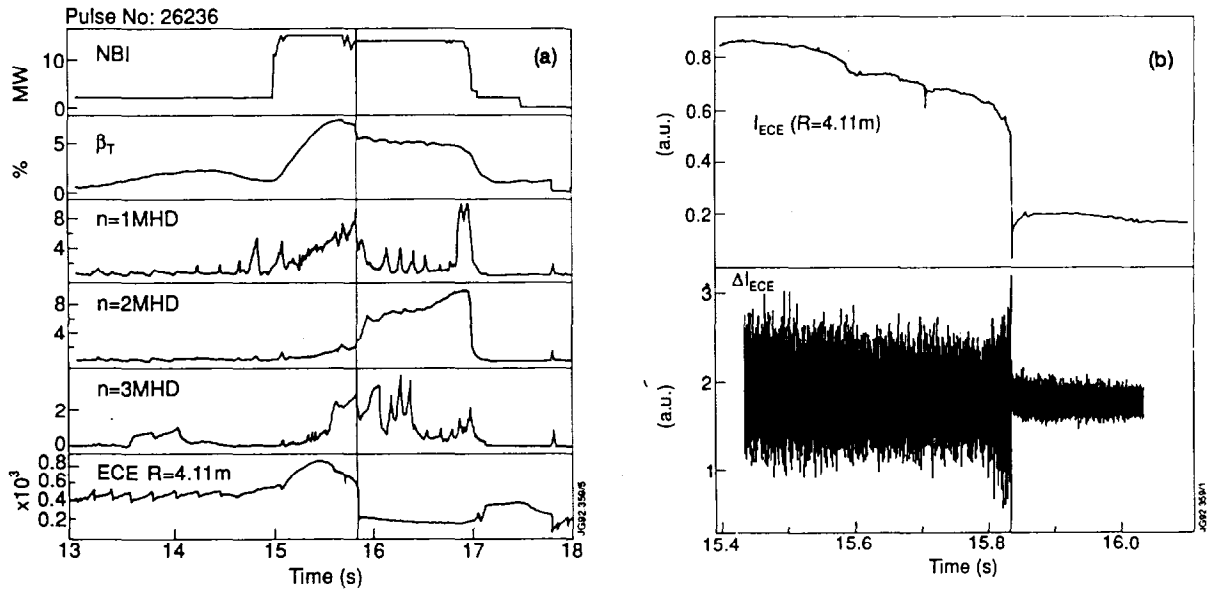

Figure 9: Overview of signals from a high-β discharge. Part (a) shows NBI power, β-toroidal, n=1,2,3 mode amplitudes and an edge ECE signal. Part (b) is an expanded view of the edge ECE around the time of the β collapse showing the increasing fluctuation level in the 20 ms period before the collapse.

Figure 9 shows a selection of signals recorded on a discharge in which the toroidal β reached 6% before collapsing. In part (a) the magnetics signals show a growing level of MHD

activity before the β collapse while the ECE signal from the plasma edge is falling. In part (b), the high-pass filtered data from the fast acquisition shows that there appears to be a rising level of fluctuations in the signal from the outermost channel (R = 4.11 m) during the last 20 ms before the collapse. This changing fluctuation level is, however, largely masked by the thermodynamic fluctuations of the black-body radiation discussed in Section 2. The magnitude of the thermodynamic fluctuations can be gauged by comparing their level before and after the collapse in T_e.

To discriminate against the broad-band noise of the thermodynamic fluctuations, and to identify any discrete MHD modes, it is useful to examine power spectra of the signals. Typically 2048 data points are included in each spectral analysis (the results of FFTs on 4 adjacent 512-point sections of the data being averaged), giving a time resolution of 10 ms. Figure 10 shows power spectra from the outermost channel (R = 4.11 m) 200 ms before the β collapse, and from three outer channels (R = 4.11, 4.06 & 3.93 m) immediately before the collapse. The onset of several modes before the β collapse is now clearly visible. The n-number identification has been made by comparing the mode frequencies with the magnetics signals. The mode at ≈23 kHz has not yet been identified.

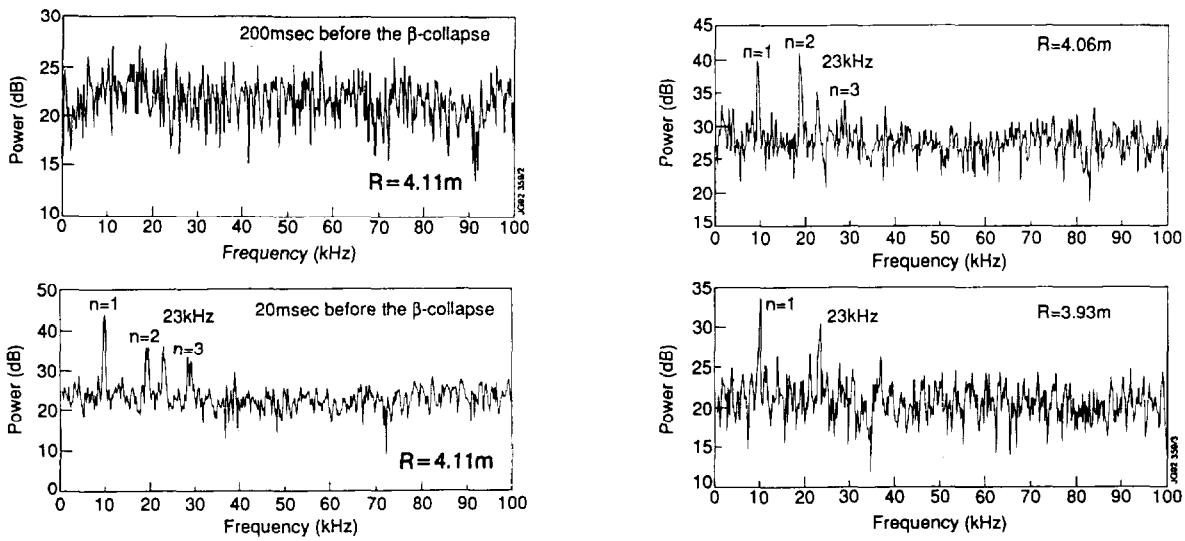

Figure 10: Power spectra of radiometer signals at times 200 ms before the β collapse (R = 4.11 m) and at 20 ms before the collapse (R = 4.11, 4.06 & 3.93 m). The n-numbers of the modes have been obtained by comparing their frequencies with the magnetics signals. The mode visible on all three channels at ≈ 23 kHz has not been identified.

A further reduction in the quantity of data to be displayed, and a better overview of the time evolution, is obtained by presenting the power spectra as contour plots in frequency-time space. This is illustrated in parts (a) and (b) of Figure 11 for the channels at R = 4.11 and R = 3.70 m. By using contour intervals linearly spaced in power spectrum level, the broad-band background can be suppressed. Finally, in Figure 11c, the data from these two channels is compressed into a single picture by plotting contours of their cross-coherence spectrum [10]. The coherence and large spatial extent of the 23 kHz mode is now clearly visible.

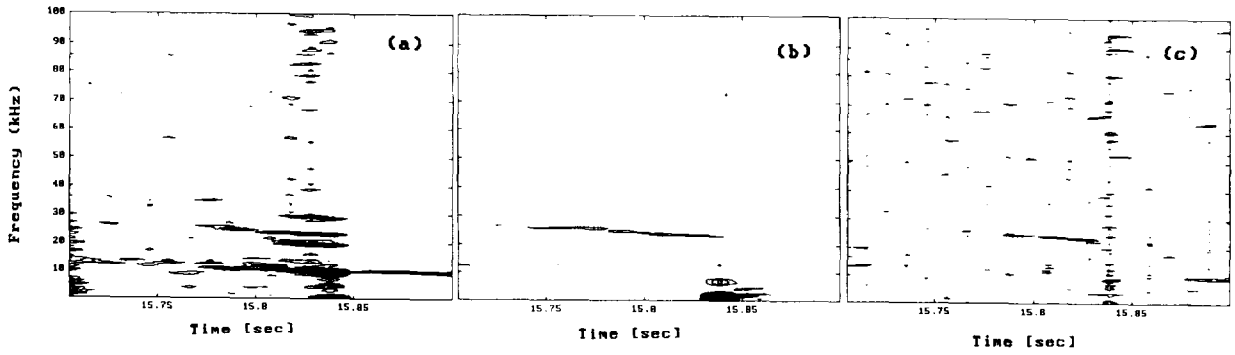

Figure 11: Parts (a) and (b) are contour plots of the power spectrum level in frequency-time space for the radiometer channels at R = 4.11 & 3.70 m. The time evolution of the modes is now visible. Part (c) shows contours of the cross-coherence spectrum for these two channels. The high degree of coherence of the 23 kHz mode across a wide spatial range is apparent.

(5) FUTURE DEVELOPMENTS

The principal improvements to the radiometer currently in progress are aimed at further enhancing its measurement capability by removing two of the limitations discussed in section 2.

The frequency coverage of the radiometer is to be increased by the addition of two further mixers which will fill the gap between the present bands 3 and 4, and extend the coverage up to 139 GHz. This will result in an almost 2:1 ratio between the high and low frequency ends of the radiometer's range, and therefore, by using both first and second harmonics, give an almost complete coverage of the outer half of the plasma for all toroidal fields between 1.7 and 3.4 tesla. To accommodate the two new mixers, two more non-polarizing beamsplitters will be added, giving a six-way division of the input radiation. By optimizing the use of a mixture of frequency selective and non-selective beamsplitters, it is hoped to achieve a throughput to the mixers about the same as the present system. We are presently examining various frequency selective beamsplitter materials.

In order to realise the spatial resolution figures given in Table I at all major radii, it is necessary to reduce the spatial volume averaged by the radiometer by improving its antenna pattern. This may also benefit studies of high order MHD modes for which the scale length in the poloidal direction may be small. These improvements will be particularly important when observing on the inboard side of the plasma (in the first harmonic) where the spot size of the existing antennas is quite large. To obtain the antenna pattern improvement, we are currently installing a Gaussian beam collection system. A pair of relay mirrors inside the vacuum vessel will focus radiation through the vacuum window and into a pair of back-to-back scalar feed horns. The small diameter constriction between the two horns will pass only the lowest order mode. However, since this constriction will have circular cross-section, both polarizations will propagate and be passed on to the oversized waveguide which transmits the radiation through the biological shield to the radiometer.

In addition to these improvements, others such as better mechanical and temperature stability (for calibration stability), and an improved fast data acquisition system, are also planned.

(6) SUMMARY

The JET ECE heterodyne radiometer has proved to be a valuable tool in the JET experimental programme. The upgraded instrument combines wide spatial coverage for a range of toroidal magnetic fields, major radius resolution of a few cm, and high sensitivity. This has been achieved by a design which employs wide bandwidth mixers with fixed frequency local oscillators. The radiometer also makes use of a combination of polarizing and non-polarizing beamsplitters to allow both first harmonic O-mode and second harmonic E-mode to be used. Areas where the radiometer could benefit from improvement have been highlighted, and those improvements currently in progress have been discussed.

The power of heterodyne radiometry as a diagnostic of fast phenomena has been illustrated by two examples. Observations of ECE from the edge region of JET H-mode discharges have shown non-thermal features which are attributed to a small population of moderately suprathermal electrons near the plasma edge. Model calculations of the steady-state emission and of the fast spikes associated with ELMs provide a consistent explanation of the observed phenomena. Measurements on high-β plasmas show how the radiometer and fast acquisition can be used to look at fast MHD phenomena. In this case it is necessary to make use of methods of presenting the large quantity of data which the instrument provides, in a way which best shows the underlying plasma behaviour.

(7) ACKNOWLEDGEMENTS

The authors wish to thank S Luckhardt and P Woskov for their contributions to the measurements of fast MHD phenomena and for the loan of data acquisition hardware. The invaluable technical assistance of H Oosterbeek is also gratefully acknowledged.

(8) REFERENCES

[1] N Salmon, D V Bartlett, A E Costley, Proceedings of the 6th International Workshop on ECE & ECRH, Culham Laboratory Report CLM-ECR (1987)

[2] A E Costley, D V Bartlett, D J Campbell, C W Gowers, D Pearson, L Porte, N Salmon, Proceedings of the 7th International Workshop on ECE & ECRH (Hefei, China, 1989)

[3] E Baker, D V Bartlett, D J Campbell, A E Costley, D Daly, A Dellis, L deKock, J Fessey, Proceedings of the 4th International Workshop on ECE & ECRH (Rome, 1984)

[4] T G Blaney, Space Science Reviews **17**, 691 (1975)

[5] K Uchino, D V Bartlett, A E Costley, N A Salmon, Proceedings of the 7th International Workshop on ECE & ECRH (Hefei, China, 1989)

[6] L Porte, D V Bartlett, D J Campbell, A E Costley, Proceedings of the 18th European Conference on Controlled Fusion and Plasma Physics (Berlin, 1991)

[7] D V Bartlett, L Porte, A E Costley, S E Jones, R Smith, A Zolfaghari, Proceedings of the 19th European Conference on Controlled Fusion and Plasma Physics (Innsbruck, 1992)

[8] L Porte, PhD thesis, University of Strathclyde (1992)

[9] P P Woskov et al, Rev. Sci. Instrum., **61**, 2995, (1990).

[10] J S Bengdat and A G Piersol, "Engineering Applications of Correlation and Spectral Analysis", Wiley, New York (1980)